Absorption lines of F centers in MgO and CaO through time-dependent hybrid-functional theory calculations

Mathilde L. D. Franckel [1,*] Stefano Falletta [1] Wei Chen [1,2] and Alfredo Pasquarello [1,†]

[1]*Chaire de Simulation à l'Echelle Atomique (CSEA), Ecole Polytechnique Fédérale de Lausanne (EPFL), CH-1015 Lausanne, Switzerland*

[2]*Institute of Condensed Matter and Nanoscience (IMCN), Université catholique de Louvain, Louvain-la-Neuve 1348, Belgium*

(Received 26 March 2025; revised 5 August 2025; accepted 14 August 2025; published 4 September 2025)

We investigate the absorption spectra of the F centers in MgO and CaO using material-specific hybrid functionals combined with time-dependent hybrid-functional theory calculations. Our study accounts for electron-hole interaction, zero-phonon renormalization, and finite-size effects, which are all found to contribute to the achieved accuracy. The spectra of the neutral states solely present absorption lines stemming from internal defect-to-defect transitions without involving conduction band states of the host. At variance, the spectra of the singly positively charged states show two lines, one analogous to those seen in the neutral states and an extra line corresponding to electron excitations from the valence band to the unoccupied defect level in the band gap. In MgO, the three transition energies pertaining to these two charged states are found to coincide, but are spread out in the case of CaO. The agreement with the energies of experimental lines is excellent, indicating that our scheme reaches an accuracy of 0.2 eV or better.

DOI: 10.1103/d78q-93fc

I. INTRODUCTION

F centers are intrinsic point defects belonging to the broader group of color centers, which are described extensively in the literature for their optical properties [1–4]. Their name derives from the German word "Farbe" meaning color [5] and specifies that these defects absorb in the visible light. In metal oxides, F centers correspond to oxygen vacancies of the crystal lattice [6]. The vacancy can be filled by a variable number of electrons, giving rise to F^0, F^{+1}, and F^{+2}, depending on the charge state of the defect. The F^0 and F^{+1} centers in metal oxides initially attracted a great deal of attention both in theoretical [7–9] and experimental [10] studies for their possible application in tunable visible lasers [11–13], but unsatisfactory results were obtained in the case of MgO and CaO [14]. More recently, it has been found that F centers in MgO play a role in the deterioration of magnetic tunnel junctions used in the field of information storage [15]. Besides their role in potentially useful applications, one of the primary motivations for the investigation of these defects rests on the simplicity of the underlying atomic structures, thereby serving as ideal benchmark systems for theoretical approaches [16–22].

The absorption spectra of F centers generally provide clearly identifiable signatures. In MgO the optical transition energies of F^0 and F^{+1} correspond to two intense broad absorption bands very close in energy, at 5.02 and 4.92 eV [14]. At variance in CaO, the transition energies related to the F^0 and F^{+1} centers differ by 0.55 eV and occur at 3.10 and 3.65 eV, respectively [14]. In comparison to the neutral and singly positive charge states, optical transitions pertaining to F^{+2} centers have not been identified, whereby their characterization has remained elusive [19].

Despite sustained efforts, a fully consensual theoretical description of the F center in MgO has yet to be reached [23–26]. In the 1990s, Illas and Pacchioni explored this system using cluster model calculations [27]. However, the transitions associated with F^0 and F^{+1} were overestimated by over 1 eV. Subsequently, Sousa and Illas highlighted the need for extensive basis sets and large cluster sizes [20]. Using many-body perturbation theory in the GW approximation, Rinke *et al.* have interpreted the optical absorption lines for the F center in MgO in terms of vertical transitions between defect states and band edges [16]. In particular, they identified at ∼3.6 eV a transition in the minority spin channel, which could serve the purpose of distinguishing F^{+1} from F^0 in an unambiguous way. However, this transition has so far not been detected experimentally. Using quantum Monte Carlo methods, Ertekin, Wagner, and Grossman then found good agreement with experiment for absorption lines involving transitions of defect electrons to the conduction band edge [18]. However, this work did not address transitions from the valence band. Strand *et al.* described the absorption lines involving the defect state through time-dependent hybrid functional theory (TDHFT) [19]. In particular, they assigned the F^0 and F^{+1} lines to internal defect transitions. Furthermore, they found the minority spin transition in F^{+1} to occur at an energy higher by 0.6 eV compared to the corresponding majority spin transition [19]. This is at variance with the work of Rinke *et al.* where these two transitions were found in an inverted order [16]. More recently, Vorwerk and Galli addressed the O vacancy in MgO employing an embedded formalism based on the Bethe-Salpeter equation (BSE) [22]. Supporting the assignment of Strand *et al.* [19], they assigned

*Contact author: mathilde.franckel@epfl.ch
†Contact author: alfredo.pasquarello@epfl.ch

the 5.02 eV absorption peak to an internal defect excitation of F^0, but it remained unclear whether band-to-defect transitions contribute to the origin of the F^{+1} line at 4.95 eV [14].

Overall, these previous theoretical investigations point out that the study of F centers in oxides is particularly challenging for a variety of reasons. These include the difficulty for an electronic-structure scheme to describe both localized defect states and delocalized band-edge states at the same level of accuracy [16,18,19,22], the significant role of finite-size effects, which should be overcome either by extrapolation procedures [19,22] or by correction schemes [16], and the necessity of accessing optical spectra, both to discard forbidden transitions [22] and to account for electron-hole interactions [16,19,22].

The theoretical study of the F center in CaO has received less focus, and the overall description of the absorption lines has not reached the level of attention devoted to the same defect in MgO [28,29]. However, the absorption lines of F^{+1} and F^0 show a larger separation in CaO, thereby facilitating the comparison with experiment. Given the occurrence of several transition lines with similar energy in MgO, a combined study addressing both the F centers in MgO and CaO would be particularly convincing for identifying a valid interpretation scheme. Furthermore, such a study would constitute a formidable benchmark for establishing the accuracy of current computational methodologies.

In this work, we investigate the absorption lines of the F centers in both MgO and CaO through time-dependent hybrid functional theory. We adopt material-specific hybrid functionals that reproduce the band gaps of the pristine system and closely satisfy the piecewise linearity condition of the exact density functional [30]. First, we calculate vertical transition energies between defect and band-edge levels for the ground-state configurations pertaining to the three charge states. From the calculated transitions, we infer that this interpretation scheme is insufficient to explain the experimental absorption lines. Next, we employ a scheme based on time-dependent hybrid functional theory that accounts for electron-hole interactions and allows one to identify the relevant transitions in terms of the underlying energy levels. We find that the absorption lines in F^0 and in the majority spin channel of F^{+1} correspond to transitions from s-like defect states within the band gap to defect states of p-like symmetry above the conduction band edge. At variance, the absorption lines in the minority spin channel involve transitions from valence-band states to the defects states in the band gap. On the basis of this understanding, all the relevant electron-hole interactions can be extracted. To account for finite-size effects, all the calculations are performed for large simulation cells and then extrapolated to the dilute limit. The calculated absorption lines associated with F^0 and F^{+1} in both MgO and CaO are found in good agreement with experiment. The successful description achieved in this work supports the adopted methodology for the interpretation of defect absorption lines.

The paper is organized as follows. In Sec. II we describe the computational setup adopted in this work. In Sec. III we set the parameters for the material-specific hybrid functionals and discuss benchmark calculations of band gaps for the pristine systems. The defect energy levels of the F centers are then studied in Sec. IV. In Sec. V we address optical transitions through the use of time-dependent hybrid functional theory and provide a comprehensive interpretation of the experimental lines. Moreover, we extract the exciton binding energies for the absorption lines associated with all the charge states of the F centers. In Sec. VI we draw the conclusions of our work.

II. METHODOLOGY

It is notoriously challenging to accurately quantify band gaps in insulators using semilocal density functional theory because of the absence of the derivative discontinuity [31,32]. Consequently, the band gaps can be undervalued by several electron volts, making it difficult to accurately position the defect levels with respect to the band edges. Possible transitions in the F center involve either the conduction or the valence band states. To address this issue, we here employ the one-parameter hybrid functional PBE0(α) [33] for the electronic-structure calculations. The mixing parameter α corresponds to the fraction of semilocal Perdew-Burke-Ernzerhof (PBE) exchange [34] that is replaced by nonlocal Fock exchange. Particular care should be taken to ensure that the chosen α correctly reproduces the energy levels of the localized defect and the delocalized band states. For large band-gap materials, standard hybrid functionals, such as PBE0(0.25) and HSE06 [35,36], are known to yield poor accuracy [37–39]. For higher accuracy, it is necessary to resort to material-specific settings of the mixing parameter. We adopt the practice of tuning the mixing parameter to the value α_{g}, which ensures that PBE0(α_{g}) closely reproduces the experimental band gap. This condition can easily be achieved since the band gap is severely underestimated at $\alpha = 0$ (i.e., with PBE) and increases linearly with α [40]. Besides describing properly the relative position of band levels, such a setting generally also yields accurate absolute energy levels of delocalized states, as demonstrated for ionization potentials [41,42], defect levels [43], and redox levels at aqueous semiconductor surfaces [44]. The choice of setting $\alpha = \alpha_{\mathrm{g}}$ can be justified by remarking that the functional PBE0(α_{g}) closely satisfies the condition of piecewise linearity of the total energy as a function of electron occupation [45], which stems from the exact density functional [30]. Through Janak's theorem [46], this condition further implies that the generalized Kohn-Sham energy levels remain constant upon electron occupation.

In wide band-gap materials such as MgO and CaO, an additional complication arises insofar as these materials are subject to significant zero-point renormalization (ZPR) due to electron-phonon interaction. In this work, the effects of phonons on the band-edge levels are taken into account by correcting them with ZPR values available in the literature. In the determination of α_{g}, the ZPR corrections need to be accounted for upon matching the calculated band gap with the experimental one. We use the ZPR values calculated by Miglio *et al.* within a nonadiabatic treatment of the phonon coupling [47]. The utilized ZPR values for MgO and CaO are given in Table I. For the same materials, Engel *et al.* [48] calculated band-gap renormalizations differing by less than 20 meV from those found by Miglio *et al.* [47], thereby providing strong support to these corrections.

For estimating the effect of zero-point motion on the defect energy levels in MgO, we adopt the scheme proposed by

TABLE I. Zero-point renormalization corrections applied in this work to the valence (ϵ_v^{ZPR}) and conduction band edges (ϵ_c^{ZPR}). The ensuing band gap correction ($E_g^{ZPR} = \epsilon_c^{ZPR} - \epsilon_v^{ZPR}$) is also given. The corrections are taken from Ref. [47]. Throughout this work, these corrections are systematically applied to the calculated band edges and band gaps. All energy corrections are given in eV.

	ϵ_v^{ZPR}	ϵ_c^{ZPR}	E_g^{ZPR}
MgO	0.32	−0.21	0.53
CaO	0.21	−0.13	0.34

Zacharias and Giustino [49,50] using a simplified phonon model based on the radial displacements of the Mg atom facing the vacancy. These motions correspond to optical modes, for which we take the frequency of 19 THz as representative of the experimental optical phonon band [51–53]. In this way we derive a spatial width of $\sigma_{ZPR} = 0.06$ bohr. Taking corresponding Gaussian variates for the radial displacements of the six Mg atoms surrounding the vacancy, we find that the distribution of the energy level of the s-like defect state shows a broadening of 0.31 eV. To evaluate the dependence on the frequency, we probe a value reduced by 10% (17 THz) finding an increased broadening of 0.45 eV. However, the mean value of the distribution of the energy level is found to be unaffected within 0.1 eV for both frequencies. In CaO, the heavier mass of the Ca atom is expected to reduce this estimate even further. In the following of our study, we thus neglect the effect of the phonon coupling on the defect levels.

In this study, the defect is described through the use of periodically repeated supercells. In the case of charged systems, a uniform background charge is used to achieve charge-neutral supercells. The interactions between periodic images and with the background charge lead to spurious finite-size effects, which vanish in the limit of infinitely large supercells. In the case of MgO and CaO, finite-size effects are particularly important because of the low dielectric constants of these materials. To correct the defect levels, we carry out calculations for supercells of increasing size and extrapolate to the dilute limit [54–58].

In state-of-the-art calculations based on many-body perturbation theory, the optical spectra are obtained solving the BSE [59–63]. However, the high computational cost of such methods makes their use prohibitive in large systems. Alternatively, methods based on TDHFT have been shown to produce optical spectra of crystalline solids in very good agreement with those obtained by solving the BSE [64,65]. To ensure such an agreement, the long-range fraction of Fock exchange appearing in the hybrid functional should correspond to the inverse high-frequency dielectric constant ϵ_∞^{-1} [64,65]. The TDHFT calculations account for the electron-hole interaction upon excitation. This leads to transition energies occurring at lower values compared to the separation between initial and final states. They occur for band-to-band transitions (free excitons), for defect-to-band and band-to-defect transitions (bound excitons), and for internal defect-to-defect transitions.

Computational details

In this work the calculations are primarily performed using the CP2K suite of codes [66]. The core-valence electronic interactions are described using Goedecker-Teter-Hutter pseudopotentials [67]. In the adopted pseudopotentials, only the electrons in the outer shell are included among the valence electrons, i.e. six electrons for O and two for Mg and Ca. We use MOLOPT Gaussian basis sets [68] and the Brillouin zone is sampled at the sole Γ point. The energy cutoff for the plane waves is set to 800 Ry.

The band structures of the pristine systems are obtained with the QUANTUM-ESPRESSO suite of codes [69]. The calculations are performed for the primitive unit cell and the Brillouin zone is sampled through Γ-centered $6 \times 6 \times 6$ **k**-point meshes. The optimized norm-conserving Vanderbilt pseudopotentials (ONCVPSP) [70] generated by the PseudoDojo framework [71] are used. In these calculations, the sp semicore states are included among the valence states for Mg and Ca. The kinetic energy cutoff for the electron wave functions is set at 100 Ry, while a cutoff of 160 Ry is used for the Fock operator. The band structure is interpolated through the use of the code WANNIER90 [72].

The TDHFT spectra are obtained through the use of the code CP2K. The calculations are performed with the velocity form, suitable to be used with periodic boundary conditions. A description of this scheme can be found in Refs. [19,73]. The adopted scheme does not include corrections due to the nonlocality of the pseudopotentials, which are generally found to be small [74]. In particular, for transitions involving the O vacancy defect states, the effect of the pseudopotential nonlocality on the peak intensities can be shown to be minor. For MgO, in the calculation of the matrix elements, changes due to the nonlocality mainly arise from inside the core region of the Mg atoms facing the vacancy (pseudopotential cutoff radius of 0.74 Å), whereas the defect wave function extends over the full region of the O vacancy (radius of 2.1 Å). Considering the sheer volume effect and the variation of the s-like wave function, we estimate that the pseudopotential nonlocality affects the oscillator strengths by less than 1%.

III. SETTING OF HYBRID-FUNCTIONAL PARAMETERS

In this section we study the pristine bulk systems in order to set the values of the exchange mixing parameters α_g for MgO and CaO in our calculations. For both materials, we consider face-centered cubic lattices, corresponding to the $Fm\bar{3}m$ space group. We take experimental lattice parameters, i.e., $a_{MgO} = 4.207$ Å, $a_{CaO} = 4.803$ Å [75]. Since this work focuses on providing a quantitative description of optical transitions, it was deemed preferable to use experimental rather than theoretical equilibrium constants. This approach is commonly adopted when evaluating the ability of electronic structure methods to reproduce band-gap excitations in solids [38,76,77].

The mixing parameters are set to produce a good description of the fundamental and optical band gaps of the materials under consideration. Through a guess-and-error procedure, we set the mixing parameters at $\alpha_g = 0.38$ for MgO and $\alpha_g = 0.34$ for CaO (cf. Table II). The accuracy of the description

TABLE II. Fractions of Fock exchange resulting from various conditions: closely reproducing the experimental band gaps given in Table III (α_g), satisfying the piecewise linearity condition (α_K), and originating from the experimental refraction index (α_ϵ). The refractive indices $n = 1.72$ for MgO [78] and $n = 1.83$ for CaO [79] are used to provide an estimate for $\alpha_\epsilon \cong n^{-2}$.

	α_g	α_K	α_ϵ
MgO	0.38	0.36	0.34
CaO	0.34	0.33	0.30

achieved is illustrated below through the comparison between calculated and experimental band gaps.

MgO has a direct band gap at Γ. We consider supercells containing 216, 512, and 1000 atoms and calculate the fundamental band gap with the hybrid functional PBE0(0.38) (Table III). We find that a linear extrapolation in L^{-1} provides a good description of the calculated band gaps as a function of the supercell size L. The band gap extrapolated to infinite cell size is 7.71 eV, within less than 0.1 eV from the experimental values at 7.83 [80] and 7.78 eV [10]; see Table III. Using TDHFT calculations, we also obtain the optical band gap for the same set of supercells. In this case, the linear extrapolation in L^{-1} yields a slightly negative excitonic binding energy. Hence, we adopt a scheme in which the exciton binding energy is extrapolated through a decaying exponential function to account for the interaction between the exciton wave function and its images [57]. This procedure yields an extrapolated binding energy of 87 meV in excellent agreement with the measured value of 85 meV [10]. Overall, these results corroborate the setting $\alpha_g = 0.38$ for MgO.

For CaO, we proceed analogously by taking supercells containing 216, 512, and 1000 atoms. The fundamental band gap is calculated with the hybrid functional PBE0(0.34) (Table III). For CaO, the band gap is indirect, corresponding to an electronic transition from the Γ point to the X point in the Brillouin zone [81,82]. We find that the convergence as a function of supercell size is rapidly achieved, with the band gap of 6.54 eV obtained for the 512-atom supercell corresponding to the converged value. However, we have not been able to find an experimental value of the indirect band gap in the literature to validate our setting of α_g. In the imaginary part of the dielectric function, the first observed transition corresponds to the direct transition at the X point [10,81]. By identifying the valence and conduction band states showing the dominant contribution to the oscillator strength of this exciton, we are able to extract the direct band-to-band transition at the X point (Table III). For the largest considered supercell of 512 atoms, we obtain an excitonic transition at 6.80 eV and a direct band-to-band transition at 7.00 eV, to be compared with the corresponding experimental values at 6.82 and 6.88 eV [81]. This agreement with the experimental characterization is largely satisfactory with deviations of only ∼0.1 eV and supports the setting of $\alpha_g = 0.34$ for CaO. For the 1000-atom supercell, we are unable to obtain transitions pertaining to the X point in our TDHFT calculations, because of the prohibitively large number of lower-lying transitions originating from the valence band states close to the Γ point. In the absence of the data point for the 1000-atom supercell, we refrain from carrying out extrapolations to infinite supercells. Given the small differences between the results for 216-atom and 512-atom supercells, we consider the latter results to be converged. This is consistent with previous studies, in which the exciton transition in MgO was found to vary by at most 0.1 eV going from 512-atom to 1000-atom supercells [19].

For reference, we provide in Fig. 1 the dispersion of the energy levels for MgO and CaO along specific lines in the Brillouin zone, as calculated with the code QUANTUM-ESPRESSO. These results are obtained through the use of hybrid functionals PBE0(α_g), in which the mixing parameters α_g are set as specified in Table II. The calculated band structure clearly shows that MgO has a direct band gap at the Γ point

TABLE III. Fundamental (E_g) and optical (E_g^{opt}) band gaps of MgO and CaO. Calculated transitions for supercell sizes with increasing number of atoms are extrapolated to infinite cell size (∞) and compared with experimental values. The points of the Brillouin zone involved in the transitions are specified. Calculated band gaps include ZPR corrections. Energies are in eV. In these calculations, the Brillouin zone is sampled at the sole Γ point.

	Supercell size				Expt.
	216	512	1000	∞	
MgO					
E_g (direct, Γ)	7.83	7.83	7.81	7.71	7.78[b]
E_g^{opt} (direct, Γ)	6.91	7.32	7.41	7.62	7.67[a], 7.70[b]
CaO					
E_g (indirect, $\Gamma \to X$)	6.59	6.54	6.54	6.54	
E_g (direct, X)	7.01	7.00	–		6.88[c]
E_g^{opt} (direct, X)	6.67	6.80	–		6.82[c]

[a]Reference [80].
[b]Reference [10].
[c]Reference [81].

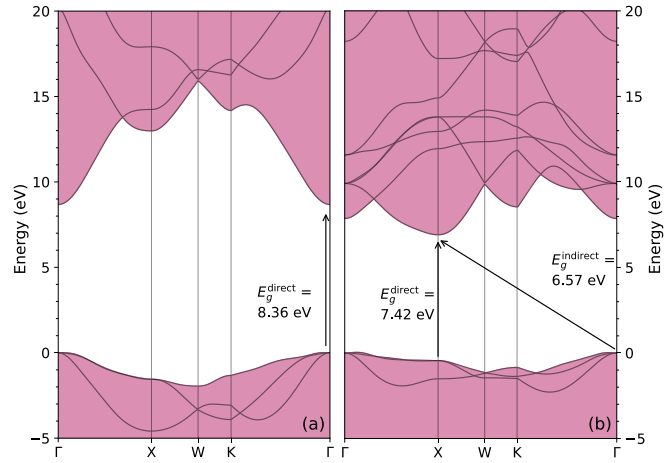

FIG. 1. Energy bands of (a) MgO and (b) CaO, calculated along high-symmetry lines at the PBE0(α_g) level with the code QUANTUM-ESPRESSO. We have applied rigid shifts of 0.44 and 0.03 eV to the conduction bands of MgO and CaO, respectively, to ensure that the band gaps correspond to the converged values obtained with the code CP2K (cf. Table III).

in the Brillouin zone [Fig. 1(a)]. At variance, the band gap of CaO is indirect, with the top of the valence band at the Γ point and the bottom of the conduction band at the X point. In CaO, the lowest direct transition occurs at the X point, as indicated by the vertical arrow in Fig. 1(b). The fundamental band gaps obtained with the code QUANTUM-ESPRESSO are 8.15 eV for MgO and 6.57 eV for CaO, to be compared with the respective extrapolated values of 7.71 and 6.54 obtained with CP2K. In the case of CaO, the two codes give the same band gap within 0.03 eV. However, in the case of MgO, the difference amounts to ∼0.4 eV, which should be attributed to the different computational setups. In Fig. 1, we have rigidly shifted the conduction band energies to reproduce the CP2K band gaps given in Table III for a consistent illustration of our results.

It is of interest to establish by how much the adopted mixing parameters α_g differ from those leading to piecewise linear functionals (α_K). We determine the mixing parameters α_K through the use of a defect state as described in Ref. [45]. For this, we take the structural configuration corresponding to the neutral state of the O vacancy, and calculate the defect Kohn-Sham levels for the neutral and positively charged states. This calculation is performed with the hybrid functional PBE0(α) for varying α. The sought-after α_K is found when the eigenvalues of the two charge states coincide, corresponding to the generalized Koopmans' condition. Upon enforcing this condition, it is important to include finite-size corrections to the calculated eigenvalues [83]. We find $\alpha_K = 0.36$ for MgO and $\alpha_K = 0.33$ for CaO. Our values of α_K agree with previous estimates of 0.34–0.38 for MgO [38,84] and 0.29 for CaO [38], found adopting similar criteria but other defect probes. The calculated α_K parameters are also close to $\alpha_g = 0.38$ for MgO and $\alpha_g = 0.34$ for CaO, adopted here to ensure an accurate band-gap description (see Table II). Hence, this result further strengthens the setting of mixing parameters made in this work. More generally, this further confirms that hybrid functionals reproducing the band gap are also close to satisfying the piecewise linearity condition [45]. The parameters α_K have been added to Table II.

An alternative way to set the mixing parameters consists in taking $\alpha_\epsilon = \epsilon_\infty^{-1}$ [85,86]. This choice properly describes the long-range potential [87] and has motivated the development of dielectric-dependent hybrid functionals [39,76,88]. For MgO and CaO, we estimate the high-frequency dielectric constant from the refractive indices n through $\epsilon_\infty \cong n^2$. We take experimental values, *viz.*, $n = 1.72$ for MgO [78] and $n = 1.83$ for CaO [79], resulting in $\alpha_\epsilon = 0.34$ for MgO and $\alpha_\epsilon = 0.30$ for CaO. The parameters α_ϵ and α_g are close differing by only 0.04 for the two materials (cf. Table II). This agreement ensures that the TDHFT calculations based on the hybrid functionals PBE0(α_g) yield a good description of the absorption spectra [64,65].

From this analysis, we infer that the mixing parameters $\alpha_g = 0.38$ for MgO and $\alpha_g = 0.34$ for CaO ensure that, in addition to reproducing the band gap the corresponding functionals also closely satisfy general properties of the exact density functional, such as the piecewise linearity and the long-range dependence of the potential. It has been found that these properties concurrently yield good structural properties across a large variety of materials [45,76,88]. In particular, the lattice parameters of MgO and CaO, are found in excellent agreement with experiment [41,76]. Hence, the overall good agreement between the parameters α_g, α_K, and α_ϵ sets the stage for a reliable baseline to investigate the various charge states of the F center in these materials.

TABLE IV. Distances (in Å) between the center of the O vacancy and its closest metal atoms for the three charge states of the vacancy, F^0, F^{+1}, and F^{+2}, compared with the metal-oxygen bond length in the pristine bulk [75]. Reported values correspond to the largest supercell of 1000 atoms.

	Bulk	F^0	F^{+1}	F^{+2}
MgO	2.10	2.10	2.19	2.22
CaO	2.40	2.46	2.56	2.63

IV. DEFECT ENERGY LEVELS

The experimentally observed F centers are assumed to originate from oxygen vacancies [6,14,25,89]. To model this defect center, we remove one O atom from the pristine bulk structures studied in Sec. III. Three charge states are considered. In the neutral state F^0, two electrons occupy a localized state of s symmetry at the site of the vacancy showing an electronic level in the band gap. We also consider the +1 and +2 charge states, denoted F^{+1} and F^{+2}, respectively, in which these two electrons are sequentially removed. In the F^{+1} state, the two spin channels exhibit different occupations, requiring the use of spin-polarized calculations.

We obtain the ground-state defect structure for each charge state through full structural relaxations. The geometrical optimization is performed at the semilocal PBE level of theory [34], since it is well documented in the literature that the use of hybrid functionals would not lead to a useful benefit for the electronic-structure properties [90,91]. We checked this explicitly for 216-atom supercells of MgO by carrying out relaxations at the hybrid-functional level of theory. Mg-Mg distances change negligibly, differing by 0.3%, 0.6%, and 1.4% for F^0, F^{+1}, and F^{+2}, respectively (see Supplemental Material (SM) [92]), while calculated defect levels remain within 0.1 eV.

In Table IV we report the distances between the center of the oxygen vacancy and its closest metal atoms in the three charge states in comparison with the metal-oxygen bond length in the pristine bulk [75]. The values given correspond to the largest supercells of 1000 atoms. In F^0, the replacement of an O^{2-} ion with two electrons in a localized s-like state essentially does not lead to any displacement of the metal cations in MgO, but produces a slight outward displacement by 0.06 Å in CaO. For F^{+1} and F^{+2}, the outward displacement is found to increase as the number of electrons trapped in the vacancy diminishes, which can be explained in terms of electrostatic interactions. The cation displacements in CaO are larger than the corresponding ones in MgO, but both follow the same trend. The Mg displacements in Table IV agree within 0.04 Å with those found previously [16,19], further supporting the robustness of the achieved structures.

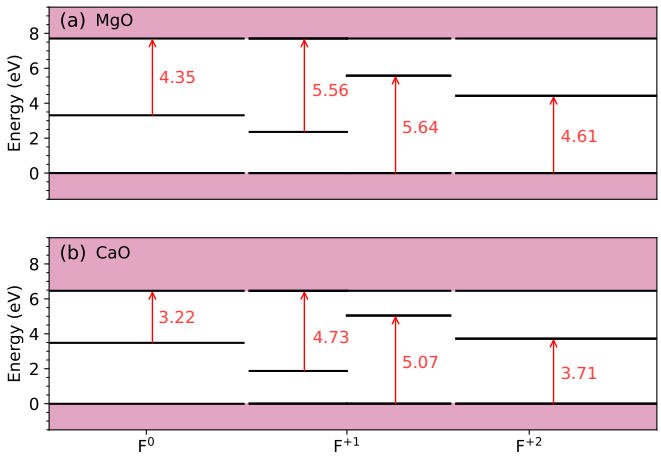

FIG. 2. Electronic transitions (red arrows with labels in eV) between defect levels and band-edge levels for various charge states of the F center in (a) MgO and (b) CaO. The F center is denoted F^0, F^{+1}, and F^{+2} depending on its charge state. The defect energy levels and transitions result from generalized Kohn-Sham eigenvalues obtained with the hybrid functional PBE0(α_g), as extrapolated to the dilute limit. For each charge state, the levels in the two spin channels are shown. The band edges have been corrected for the ZPR effect (see Table I).

We calculate the generalized Kohn-Sham energy levels associated with the various charge states of the F centers in MgO and CaO for all the considered supercells. We then extrapolate the defect energy levels to the dilute limit, assuming a L^{-1} dependence. The extrapolated energy levels together with transitions to the band edges are reported in Fig. 2.

For the neutral charge state F^0, there is a perfect equivalence between the two available spin channels. We find a defect level in the band gap at 4.35 and 3.22 eV below the conduction band for MgO and CaO, respectively. The only possible optical transitions involving the defect correspond to excitations from the defect state to the unoccupied states in the conduction band.

In the defect state F^{+1}, the defect level in the majority spin channel α is occupied and lies in the band gap at 5.56 eV from the conduction band in MgO. In CaO the corresponding defect level lies at 4.73 eV from the conduction-band edge. Similar to F^0, the electron in this state can be excited to the unoccupied states in the conduction band. In the minority spin channel β, the F^{+1} state presents an unoccupied state in the band gap at 5.64 eV above the valence band in MgO and at 5.07 eV above the valence band in CaO. This defect state can accept electrons excited from the occupied states in the valence band. In the following, we distinguish transitions occurring in the α and β channels by adopting the notation F_α^{+1} and F_β^{+1}.

In the F^{+2} state, the defect levels in both spin channels are unoccupied. The spin equivalence is thus fully recovered. Only electronic transitions from the valence band can occur at energies larger than 4.61 and 3.71 eV for MgO and CaO, respectively.

The calculated transition energies between the defect levels and the band edges do not offer a straightforward interpretation of the experimental results. In MgO, two transitions are experimentally observed at 5.02 and 4.92 eV [14]. According to the calculated values, only the two transitions associated with the F^{+1} are sufficiently large to account for the experimental observations. Indeed, we could expect that the electron-hole interaction, which has so far not been considered, would reduce the calculated transition energies, e.g., by 0.45 to 0.56 eV as estimated previously [16]. However, this interpretation remains unsatisfactory. Indeed, would the transition F_α^{+1} be responsible for one of the experimental lines, it would be unclear why the similar transition in the F^0 state would not be observable at lower energy. Similar interpretation difficulties apply to the case of CaO. Furthermore, in a recent study, it has been highlighted that transitions between the defect level and the conduction-band edge in MgO are forbidden because of the selection rule preventing optical transitions between states of s-like character [22]. These considerations weaken the interpretation of the observed lines solely in terms of defect-to-band or band-to-defect transitions. They also highlight the importance of accounting for electron-hole interactions and selection rules.

V. TIME-DEPENDENT HYBRID FUNCTIONAL THEORY RESULTS

To include in our description the effects from both electron-hole interaction upon excitation and transition matrix elements, we turn to TDHFT calculations to identify the relevant electronic transitions in MgO and CaO. We perform such calculations for the three charge states F^0, F^{+1}, and F^{+2}, obtaining the corresponding spectra for the oscillator-strength distribution. The positions of the main peaks are extracted for each of the considered supercells and extrapolated to the dilute limit assuming a L^{-1} dependence. All the extracted values are tabulated and compared with experimental results. Furthermore, to provide an interpretation of the resulting transitions, we analyze the TDHFT peaks in terms of excitation amplitudes of single-particle transitions and locate their energies in the joint density of states (jDOS).

The calculated spectra are obtained for supercell sizes of 512 atoms, which allows us to extend with a reasonable computational effort the studied range of transition energies up to 7.0 eV for MgO and up to 6.0 eV for CaO. The TDHFT spectra are corrected for both finite-size and ZPR effects. For this, the energies of the transitions involving only defect states are corrected to correspond to the energies extrapolated to the dilute limit. Energies of defect-to-band transitions are further corrected to account for the ZPR shifts of the valence band. Similarly, the jDOS is rigidly displaced to correct for these effects. The ZPR effects dominate these shifts (cf. Table I), since finite-size corrections are generally on the order of 0.1 eV.

A. MgO

For the F^0 state of the oxygen vacancy in MgO, a strong peak stands out at 4.96 eV in the oscillator strength distribution for the energy range studied [see Fig. 3(a) and Table V]. We also observe peaks of lower oscillator strength at about 5.9 eV and 6.6 eV. The position of the main peak is in excellent agreement with the values of the experimental transition at 5.01–5.03 [14,23,25]. We remark that this transition occurs at slightly larger energy than the

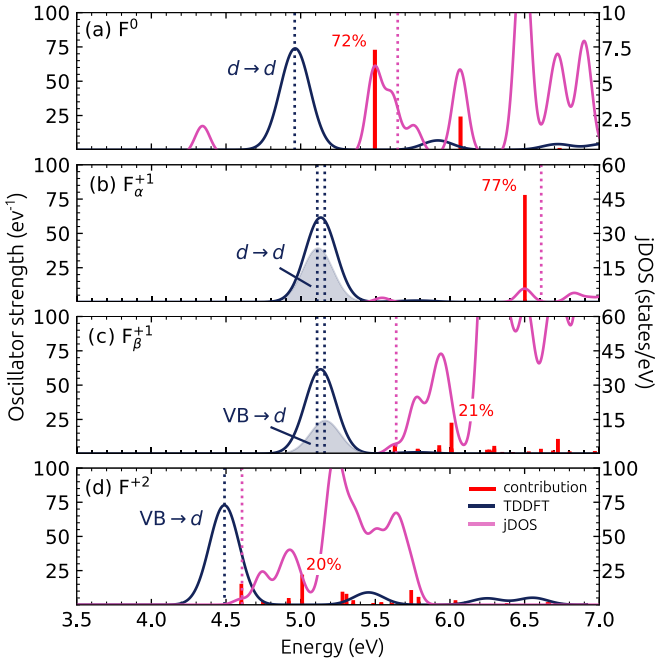

FIG. 3. Oscillator strength distribution (black) and joint density of states (jDOS, pink) associated with oxygen vacancies in MgO in the (a) F^0, (b) F^{+1} with shaded area from $d \rightarrow d$ transitions and jDOS in the majority spin channel α, (c) F^{+1} with shaded area from VB $\rightarrow d$ transitions and jDOS in the minority spin channel β, and (d) F^{+2} states. The main absorption lines (black dotted), and the reference energies for the exciton binding energies (pink dotted) are indicated. The spectra are obtained for a supercell with 512 atoms but are corrected for finite-size and ZPR effects. The red bars indicate the excitation amplitudes of the marked jDOS transitions contributing to the corresponding oscillator strengths of the main peaks. A Gaussian function with a standard deviation of 0.2 eV (0.1 eV) is used for the broadening of the oscillator strength (jDOS).

defect-to-band separation found at 4.35 eV. This is seen in Fig. 3(a), where the TDHFT peak appears beyond the onset of the jDOS. The transitions at the onset of the jDOS do not contribute to the oscillator strength of the observed peak, since these single-particle excitations correspond to forbidden transitions between the s-like defect state in the band gap and the s-like states at the edge of the conduction band [22]. The analysis of the single-particle excitation amplitudes contributing to the observed peak reveals that the dominant contribution, corresponding to 72% of the oscillator strength, is due to transitions occurring at ∼5.5 eV in the jDOS. By visual inspection, we identify the relevant final states as a triplet of defect states of p-like symmetry being resonant with the conduction band, in agreement with the assignment made previously by Strand *et al.* [19]. This provides strong evidence for the interpretation of the main peak in terms of transitions from the defect state in the band gap to quasilocalized defect states resonant with the conduction band [22] (internal defect-to-defect transitions, $d \rightarrow d$). However, we note that the excitation amplitudes of these single particle transitions account only for 72% of the F^0 absorption line, implying that higher lying excitations are also involved.

TABLE V. Transition energies (in eV) associated with the F center in MgO and CaO as calculated with TDHFT in its various charge states and spin channels (α and β), for the supercell sizes considered in this work. The calculated values are extrapolated to the dilute limit (∞) assuming a linear dependence in L^{-1} and compared to experimental results. The F_β^{+1} transition for the 1000-atom supercell in CaO could not be obtained, hence the value corresponding to the 512-atom supercel is taken as extrapolated result and is indicated between parentheses. The F_β^{+1} and F^{+2} transitions involve valence band states as initial states and have thus systematically been reduced by $\epsilon_v^{\mathrm{ZPR}}$ to account for the ZPR shift of the valence band (0.32 eV for MgO and 0.21 eV for CaO; see Table I).

	Supercell size				Expt.
	216	512	1000	∞	
MgO					
F^0	5.25	5.11	5.08	4.96	5.01–5.03[abc]
F_α^{+1}	5.10	5.06	5.07	5.11	4.92[ac], 4.96[b]
F_β^{+1}	4.99	5.03	5.06	5.16	
F^{+2}	4.45	4.49	4.49	4.49	
CaO					
F^0	3.18	3.10	3.11	3.16	3.10[c], 3.1[d]
F_α^{+1}	3.48	3.46	3.45	3.45	3.65[c], 3.6[d]
F_β^{+1}	4.52	4.56	–	(4.56)	4.8[d]
F^{+2}	3.62	3.65	3.65	3.63	

[a]Reference [25].
[b]Reference [23].
[c]Reference [14].
[d]Reference [89].

For the F^{+1} state, the spin majority channel α shows a peak at 5.11 eV [Fig. 3(b)] corresponding to an internal defect-to-defect transition, analogous to that found for the F^0 state. In the minority spin channel F_β^{+1} [Fig. 3(c)], we distinguish a peak at 5.16 eV originating from transitions from the valence band to the unoccupied defect state, i.e., VB $\rightarrow d$. The oscillator strength of this transition is comparable to that in the spin channel α, carrying about 60% of its intensity. We remark that the VB $\rightarrow d$ transition in the F_β^{+1} spectrum draws oscillator strength from throughout the valence band, as seen from the location of the red bars in Fig. 3(c). Thus, it is no longer possible to associate a dominant single-particle transition with this peak.

Hence, our study indicates that the transition in the F_α^{+1} excitation channel at 5.11 eV essentially coincides with that in F_β^{+1} channel at 5.16 eV, giving rise to a single peak in the F^{+1} spectrum. These calculated transition energies are in very good agreement with the experimental peak for the F^{+1} state found at 4.92–4.96 eV [14,23,25]. Thus, our results provide clear support to the suggestion that the experimental peak for F^{+1} could be composed of two distinct contributions, explaining in this way its asymmetric shape [23] and the creation of holes upon excitation with 5 eV light [93]. Strand *et al.* [19] already hinted at this interpretation although the F_α^{+1} and F_β^{+1} transitions were found to be separated by as much as 0.6 eV in their calculation. At variance, Rinke *et al.* found the transition in the F_β^{+1} channel at 3.6 eV [16], i.e., at 1.5 eV lower energy than the transition calculated in this work. Their setup being based on many-body perturbation

theory and small supercells, it is difficult to clearly establish the reason for this discrepancy.

The calculated spectrum for the F^{+2} state shows a single peak at 4.49 eV [see Fig. 3(d) and Table V], corresponding to transitions from the valence band to the unoccupied defect state in the band gap, VB $\rightarrow d$. These excitations are analogous to those in the F_β^{+1} channel, by which single-particle transitions involving states throughout the valence band lend oscillator strength to the absorption line. So far, no experimental absorption line associated with the F^{+2} state has been detected. From the calculated formation energies vs Fermi energy (see SM [92]), we infer that the F^{+2} state is the most stable charge state for low Fermi energies in the band gap, namely up to 3.0 eV above the valence band edge. The absence of an experimental signature might simply imply that available electronic states at these energies are easily occupied leading to low F^{+2} concentrations. However, due to the insulating nature of this material, it is not given that a description based on equilibrium Fermi energy applies. According to our calculations, the oscillator strength of the absorption line associated with the F^{+2} state is sizable. Its nondetection could then imply that the characteristic line of the F^{+2} state is hidden by those pertaining to the other charge states. The F^{+2} transition could possibly contribute to the asymmetry of the F^{+1} line [23], as suggested by Strand *et al.* [19]. However, our calculations indicate that the separation between the F^{+2} line and those of F^0 and F^{+1} amounts to at least 0.5 eV (see Table V).

In the experimental spectra [14,23,25], the main transition energies occurring in F^0 and F^{+1} are found in an inverse order with respect to our calculations. This stems from the close separation of ∼0.08 eV between the two experimental lines. From the comparison between calculated and respective measured lines, we infer that deviations amount to at most 0.2 eV, which thus sets the accuracy of our theoretical scheme. This level of accuracy provides strong support for the assignment of the optical absorption around 5 eV to O vacancy defects. Recently, this assignment has been questioned by experimental data, which highlight that there is a discrepancy between the defect concentrations inferred from optical absorption and electron-paramagnetic resonance measurements [94]. However, the disruptive irradiation conditions and the high-temperature regime in these experiments lead to the generation of a variety of defects, such as interstitials and multivacancies [94]. To fully understand these experiments, it is therefore necessary to provide a detailed theoretical modeling of the response of all potential defects to the two probes used.

It is of interest to discuss whether our calculations bring light to the assignment of the experimental absorption lines to F^0 and F^{+1} defect states. As mentioned above, the separation of the two main absorption lines is too small compared to the accuracy of our calculations, preventing discrimination in terms of calculated transition energies. As far as oscillator strengths are concerned, our results indicate that the F^0 line has a stronger oscillator strength than the F^{+1} one (with a ratio of 1.25), in qualitative agreement with experimental estimates (ratio of 1.56) [25]. However, the strongest element that allows us to support the experimental assignment of the absorption lines to F^0 and F^{+1} comes from the experimental work by Monge *et al.* [93]. Their work reveals that the selective excitation of the F^{+1} transition concomitantly leads to the generation of holes in the valence band. This observation cannot be accounted for in the case of F^0, where only excitations of electrons from the defect state are possible. In contrast, our calculations show that the mechanism is fully consistent with F^{+1}, where two distinct processes occur concurrently at the same excitation energy: an excitation from the defect state in the α spin channel, and an excitation from the valence band into the defect state in the β spin channel. Hence, our theoretical study supports the current assignment of the absorption lines to F^0 and F^{+1}.

TABLE VI. Exciton binding energies (in eV) of F center lines in MgO and CaO, as calculated for various supercell sizes. The binding energies are given with respect to a reference energy corresponding to a weighted average in the case of $d \rightarrow d$ transitions (see text) and to the onset of transitions from the band edge for VB $\rightarrow d$ transitions. The binding energy of the F_β^{+1} line for the 1000-atom supercell entry is derived assuming that the F_β^{+1} line is converged with the 512-atom supercell (indicated between parentheses). Values pertaining to VB $\rightarrow d$ transitions could be extrapolated to the dilute limit (∞). The binding energies in this table do not depend on the adopted ZPR values.

	Supercell size			
	216	512	1000	∞
MgO				
F^0	0.90	0.90	0.74	—
F_α^{+1}	1.56	1.50	1.48	—
F_β^{+1}	0.85	0.73	0.68	0.48
F^{+2}	0.65	0.42	0.36	0.12
CaO				
F^0	1.18	1.08	1.08	—
F_α^{+1}	1.87	1.83	1.82	—
F_β^{+1}	0.74	0.61	(0.59)	(0.51)
F^{+2}	0.63	0.43	0.36	0.08

It is of interest to quantify the effect of the electron-hole interaction on the calculated transition energies of the various absorption lines. For each one of these lines, the exciton binding energy is defined as the separation between the TDHFT peak and a reference energy. For defect-to-defect transitions, $d \rightarrow d$, we determine the reference energy as the average over the involved single-particle transition energies weighted by their excitation amplitudes [see Figs. 3(a) and 3(b)]. For band-to-defect transitions, VB $\rightarrow d$, the exciton binding energy of an absorption line is defined with respect to the onset of the transitions from the band edge [see Figs. 3(c) and 3(d)].

The calculated exciton binding energies are summarized in Table VI. For the $d \rightarrow d$ transitions in MgO, we experience difficulties in extrapolating the exciton binding energies to the dilute limit. This results from the sparse representation of the band states when using the sole Γ point, by which the resonance between the final states and the band states is not smoothly described for varying supercell size. However, our calculations for the three supercell sizes studied deliver a consistent description, with exciton binding energies of 0.82 ± 0.08 and 1.52 ± 0.04 eV for the F^0 and F_α^{+1} lines, respectively (cf. Table VI). The enhanced binding energy found for the F_α^{+1} line almost entirely results from a

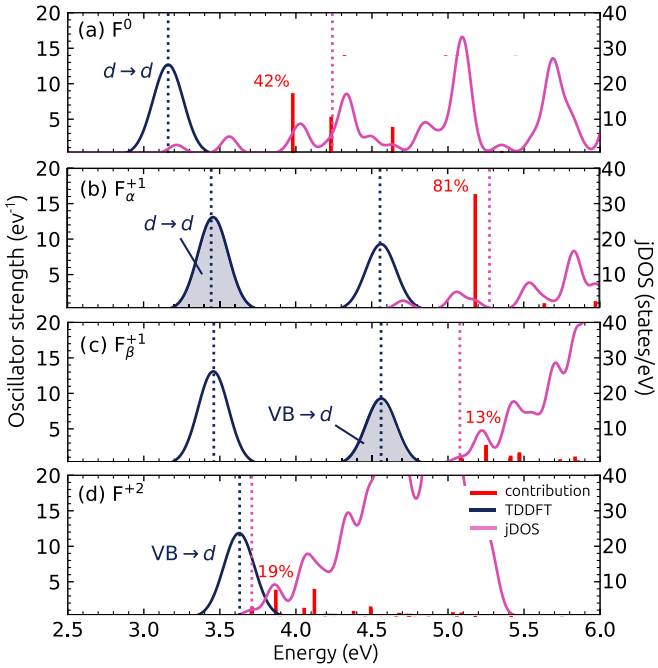

FIG. 4. Same as in Fig. 3 but for CaO.

downwards shift of the initial s-like defect level. Since the initial-state and final-state wave functions of the dominating s-p transition are found to be very similar in F^0 and F^{+1}, this result indicates that the enhanced binding energy should not be interpreted as resulting from a two-state exciton, where a single electron-hole pair dominates the excitonic state. This is confirmed in Figs. 3(a) and 3(b), where the weight of the dominating s-p transition in the F^0 and F_α^{+1} lines is found to be limited to 72% and 77%, respectively. Previous BSE calculations of the exciton binding energies for the F^0 and F_α^{+1} lines resulted in respective estimates of 0.45 and 0.56 eV [16], but were based on different reference energies. For the VB $\rightarrow$ d transitions, there were no issues for extrapolating the exciton binding energies to the dilute limit, resulting in 0.48 and 0.12 eV for the F_β^{+1} and F^{+2} lines, respectively. We use the extrapolated exciton binding energies to determine the finite-size correction to be applied to the jDOS. In the case of $d \rightarrow d$ transitions, we used the binding energy calculated for the 512-atom supercell.

B. CaO

In CaO the lines associated with the oxygen vacancy are overall very similar to those in MgO. Indeed, absorption peaks in the spin majority channel correspond to $d \rightarrow d$ transitions, whereas the relevant transitions in the spin minority channel are of the VB $\rightarrow$ d kind. The main difference with respect to the oxygen vacancy in MgO results from the energies of the absorption lines and their oscillator strengths (see Fig. 4 and Table V). In MgO, all the F center transitions fall within a small energy range, which makes the experimental identification challenging. Therefore, it is of particular interest to consider the F center in CaO and carry out a similar analysis as for the corresponding defect in MgO.

In the case of F^0, the absorption spectrum is dominated by a single line occurring at 3.16 eV [Fig. 4(a) and Table V). Similar to MgO, this transition corresponds to a $d \rightarrow d$ transition, involving final states of p-like symmetry, which dominate the excitation amplitudes at the level of 42%. In particular, we note that conduction-band edges at the X or Γ point do not contribute as final states in any relevant way. As seen in Fig. 4(a), the F^0 line in CaO occurs at slightly lower energy compared to the energy of the onset of $d \rightarrow$ CB transitions.

For the F^{+1} state, different transitions occur in the two spin channels [Figs. 4(b) and 4(c) and Table V]. In the spin majority channel α, we observe a peak at 3.45 eV [Fig. 4(b) and Table V], in good agreement with the experimental line at 3.65 eV [14,89]. In our calculations, the separation between this peak and the analogous peak in the F^0 state amounts to 0.29 eV, only slightly lower than the measured value of 0.55 eV [14,89]. In the experiment [89], the F^0 and F_α^{+1} peaks are clearly distinguishable as separate transitions, and the energy order in which they appear corresponds to that in our calculation.

In the F_β^{+1} channel, we find a peak at 4.56 eV with oscillator strength corresponding to $\sim$70% compared to the peak in the F_α^{+1} channel [Fig. 4(c) and Table V]. Thus, at variance with the description of the same charge state in MgO, the F^{+1} state in CaO gives rise to two well-separated transitions. There is no formal experimental identification of the F_β^{+1} line. However, Ward and Hensley detected a band at 4.8 eV in F^{+1}-rich CaO samples, which they tentatively attributed to an unidentified metallic impurity [89]. The good agreement between measured and calculated peak energy suggests that this band could instead correspond to the F_β^{+1} line. For the energy of the F_β^{+1} line, we rely on the calculation performed with the 512-atom supercell, since its description with the 1000-atom supercell would require a prohibitively large number of lower lying states. However, given the overall accuracy of the other lines obtained with the 512-atom supercell for CaO (cf. Table V), we estimate that residual finite-size effects are negligible.

In the F^{+2} state, a single absorption line is found at 3.63 eV [Fig. 4(d) and Table V]. This transition has so far not been detected experimentally. From the calculated formation energies, we obtain that the F^{+2} state is the most stable charge state up to 2.5 eV above the valence band maximum (see SM [92]). Analogously to MgO, the nondetection could result from the fact that this charge state easily captures electrons leading to low F^{+2} concentrations or that the characteristic F^{+2} line is indistinguishable from other transitions occurring at close energy. More specifically, this could be the F_α^{+1} channel in the latter case (cf. Table V).

The exciton binding energies as obtained for the various absorption lines in CaO are reported in Table VI. Overall, the calculated exciton binding energies follow the same trends as for MgO. For $d \rightarrow d$ transitions, the exciton binding energies amount to 1.08 eV for F^0 and 1.82 eV for F_α^{+1}, corresponding to the converged values obtained with the 1000-atom supercells. For VB $\rightarrow$ d transitions, we find extrapolated values of 0.51 and 0.08 eV for F_β^{+1} and F^{+2}, respectively.

VI. CONCLUSION

In this work, we study the absorption lines of F centers in MgO and CaO. Material-specific hybrid functionals are

constructed to optimally reproduce the defect energy levels and the band gaps. Time-dependent hybrid functional theory is used to obtain the oscillator strengths of the principal transitions, accounting in this way for transition rules and excitonic effects. Furthermore, particular care is devoted to zero-phonon renormalization and finite-size effects to achieve high accuracy in the description.

In both MgO and CaO, the F center presents the same transition kinds. In the neutral state of the F center, we find that the principal absorption line results from an internal defect-to-defect transition between the s-like state in the band gap and defect states of p-like symmetry, which are resonant with the conduction band. In the F^{+1} state, two kinds of transitions occur concurrently. First, similar to the F^0 state, one finds a defect-to-defect transition in which defect electrons are excited to defect states lying above the conduction-band edge. Second, there is an absorption line corresponding to transitions from the valence band to the unoccupied defect level in the band gap. Finally, in the F^{+2} state, only electron excitations from the valence band to unoccupied defect levels in the band gap can occur.

The pictures in MgO and CaO differ in terms of the involved transition energies and oscillator strengths. In MgO, the F^0 transition as well as the two F^{+1} transitions carry sizable and comparable oscillator strengths. There is an extraordinary coincidence of transition energies. As already pointed out in experimental work [25], the F^0 and F^{+1} lines are found at essentially the same transition energies. More interestingly, the two transitions occurring in the F^{+1} state are found to occur at coincident energies as well. This description is in agreement with hints coming from experiment, which point to an asymmetric shape of the F^{+1} line [23] and to the possibility of creating holes through excitation at the F^{+1} transition energy [93]. The F^{+2} line is found to occur at an energy lower by $\sim$0.5 eV with respect to the F^0 and F^{+1} lines. This likely indicates that this charge state of the oxygen vacancy does not occur in the experiment.

In CaO, the lines resulting from internal defect-to-defect transitions stand out in the F^0 and F^{+1} spectra. In our calculations, the transition energies of these principal lines are found to differ by 0.3 eV, in agreement with the identification of two distinguishable peaks in the experiment [89]. In the F^{+1} spectrum, the band-to-defect transition occurs at higher energy, in good agreement with that of an experimental band observed in F^{+1}-rich samples [89]. The F^{+2} line is found to occur at slightly higher energy than for F^0 and F^{+1}, but there is no indication in the experimental spectrum that this charge state occurs.

For all the observed lines in both MgO and CaO, the calculated transition energies are in excellent agreement with their experimental counterparts. This comparison with experiment suggests that the accuracy of our calculations can be quantified to be on the order of 0.2 eV or better, which is remarkable in view of the large band gaps of these materials. For this level of accuracy, it is important to concurrently account for the electron-hole interaction (up to 1.9 eV; cf. Table VI), the zero-phonon renormalization (from 0.1 to 0.3 eV; cf. Table I), and the finite-size effect (up to 0.1 to 0.3 eV depending on the supercell used; cf. Table V), since all these effects are sizable with respect to achieved accuracy. Our investigation thus confirms that the F centers in MgO and CaO constitute an excellent testbed for evaluating the performance of advanced electronic-structure methods. The achieved accuracy also supports these methods for being used more extensively in the interpretation of spectroscopic defect lines.

ACKNOWLEDGMENTS

The authors thank Giorgio Palermo and Stefan Riemelmoser for useful interactions. M.L.D.F. acknowledges support from an INSPIRE fellowship provided by the National Center of Competence in Research (NCCR) "Materials' Revolution: Computational Design and Discovery of Novel Materials (MARVEL)" of the Swiss National Science Foundation. The calculations have been performed at the Swiss National Supercomputing Centre (CSCS) (grant under project No. s1122 and No. lp60).

DATA AVAILABILITY

The atomic structures and example input files used for the calculations are freely available on the Materials Cloud platform [95].

[1] N. Itoh, Creation of lattice defects by electronic excitation in alkali halides, Adv. Phys. **31**, 491 (1982).
[2] N. Itoh and K. Tanimura, Formation of interstitial-vacancy pairs by electronic excitation in pure ionic crystals, J. Phys. Chem. Solids **51**, 717 (1990).
[3] K. Song and R. T. Williams, *Self-Trapped Excitons* (Springer, Berlin, 1993).
[4] R. Williams and K. Song, The self-trapped exciton, J. Phys. Chem. Solids **51**, 679 (1990).
[5] *Physics of Color Centers*, edited by W. B. Fowler (Academic Press, London, 1968).
[6] J. E. Wertz, P. Auzins, R. A. Weeks, and R. H. Silsbee, Electron spin resonance of F centers in magnesium oxide; Confirmation of the spin of magnesium-25, Phys. Rev. **107**, 1535 (1957).
[7] R. F. Wood and T. M. Wilson, Electronic structure of the F center in CaO, Phys. Rev. B **15**, 3700 (1977).
[8] R. Wood and T. Wilson, Electronic structure of the F-center in CaO and MgO, Solid State Commun. **16**, 545 (1975).
[9] B. M. Klein, W. E. Pickett, L. L. Boyer, and R. Zeller, Theory of F centers in the alkaline-earth oxides MgO and CaO, Phys. Rev. B **35**, 5802 (1987).
[10] R. C. Whited and W. C. Walker, Exciton spectra of CaO and MgO, Phys. Rev. Lett. **22**, 1428 (1969).
[11] B. Henderson, Tunable visible lasers using F^+ centers in oxides, Opt. Lett. **6**, 437 (1981).
[12] P. Edel, Photoluminescence of additively coloured magnesium oxide. II. Transient features in circular polarisation and opti-

cally detected magnetic resonance, J. Phys. C: Solid State Phys. **15**, 1569 (1982).
[13] W. Gellermann, Color center lasers, J. Phys. Chem. Solids **52**, 249 (1991).
[14] Y. Chen, V. M. Orera, R. Gonzalez, R. T. Williams, G. P. Williams, G. H. Rosenblatt, and G. J. Pogatshnik, Effect of substitutional hydride ions on the charge states of oxygen vacancies in thermochemically reduced CaO and MgO, Phys. Rev. B **42**, 1410 (1990).
[15] B. Taudul, M. Bowen, and M. Alouani, Impact of single and double oxygen vacancies on electronic transport in Fe/MgO/Fe magnetic tunnel junctions, J. Appl. Phys **128**, 143902 (2020).
[16] P. Rinke, A. Schleife, E. Kioupakis, A. Janotti, C. Rödl, F. Bechstedt, M. Scheffler, and C. G. Van de Walle, First-principles optical spectra for F centers in MgO, Phys. Rev. Lett. **108**, 126404 (2012).
[17] N. A. Richter, S. Sicolo, S. V. Levchenko, J. Sauer, and M. Scheffler, Concentration of vacancies at metal-oxide surfaces: Case study of MgO(100), Phys. Rev. Lett. **111**, 045502 (2013).
[18] E. Ertekin, L. K. Wagner, and J. C. Grossman, Point-defect optical transitions and thermal ionization energies from quantum Monte Carlo methods: Application to the F-center defect in MgO, Phys. Rev. B **87**, 155210 (2013).
[19] J. Strand, S. K. Chulkov, M. B. Watkins, and A. L. Shluger, First principles calculations of optical properties for oxygen vacancies in binary metal oxides, J. Chem. Phys. **150**, 044702 (2019).
[20] C. Sousa and F. Illas, On the accurate prediction of the optical absorption energy of F-centers in MgO from explicitly correlated *ab initio* cluster model calculations, J. Chem. Phys. **115**, 1435 (2001).
[21] A. Gallo, F. Hummel, A. Irmler, and A. Gruneis, A periodic equation-of-motion coupled-cluster implementation applied to F-centers in alkaline earth oxides, J. Chem. Phys. **154**, 064106 (2021).
[22] C. Vorwerk and G. Galli, Disentangling photoexcitation and photoluminescence processes in defective MgO, Phys. Rev. Mater. **7**, 033801 (2023).
[23] L. A. Kappers, R. L. Kroes, and E. B. Hensley, F^+ and F' centers in magnesium oxide, Phys. Rev. B **1**, 4151 (1970).
[24] M. Sterrer, E. Fischbach, T. Risse, and H.-J. Freund, Geometric characterization of a singly charged oxygen vacancy on a single-crystalline MgO(001) film by electron paramagnetic resonance spectroscopy, Phys. Rev. Lett. **94**, 186101 (2005).
[25] Y. Chen, J. L. Kolopus, and W. A. Sibley, Luminescence of the F^+ center in MgO, Phys. Rev. **186**, 865 (1969).
[26] J. C. Kemp, J. C. Cheng, E. H. Izen, and F. A. Modine, Magneto-optical structure of the MgO F band, Phys. Rev. **179**, 818 (1969).
[27] F. Illas and G. Pacchioni, Optical properties of surface and bulk F centers in MgO from *ab initio* cluster model calculations, J. Chem. Phys. **108**, 7835 (1998).
[28] J. Carrasco, C. Sousa, F. Illas, P. V. Sushko, and A. L. Shluger, Optical absorption and luminescence energies of F centers in CaO from *ab initio* embedded cluster calculations, J. Chem. Phys. **125**, 074710 (2006).
[29] K. Wu, T. Liu, R. Sun, J. Song, and C. Shi, First-principles calculations of oxygen vacancy in CaO crystal, Eur. Phys. J. D **74**, 209 (2020).
[30] J. P. Perdew, R. G. Parr, M. Levy, and J. L. Balduz, Density-functional theory for fractional particle number: Derivative discontinuities of the energy, Phys. Rev. Lett. **49**, 1691 (1982).
[31] J. P. Perdew and M. Levy, Physical content of the exact Kohn-Sham orbital energies: Band gaps and derivative discontinuities, Phys. Rev. Lett. **51**, 1884 (1983).
[32] L. J. Sham and M. Schlüter, Density-functional theory of the energy gap, Phys. Rev. Lett. **51**, 1888 (1983).
[33] J. P. Perdew, M. Ernzerhof, and K. Burke, Rationale for mixing exact exchange with density functional approximations, J. Chem. Phys. **105**, 9982 (1996).
[34] J. P. Perdew, K. Burke, and M. Ernzerhof, Generalized gradient approximation made simple, Phys. Rev. Lett. **77**, 3865 (1996).
[35] J. Heyd, G. E. Scuseria, and M. Ernzerhof, Hybrid functionals based on a screened Coulomb potential, J. Chem. Phys. **118**, 8207 (2003).
[36] J. Heyd, G. E. Scuseria, and M. Ernzerhof, Erratum: Hybrid functionals based on a screened Coulomb potential [J. Chem. Phys. 118, 8207 (2003)], J. Chem. Phys. **124**, 219906 (2006).
[37] W. Chen and A. Pasquarello, Band-edge levels in semiconductors and insulators: Hybrid density functional theory versus many-body perturbation theory, Phys. Rev. B **86**, 035134 (2012).
[38] J. Yang, S. Falletta, and A. Pasquarello, One-shot approach for enforcing piecewise linearity on hybrid functionals: Application to band gap predictions, J. Phys. Chem. Lett. **13**, 3066 (2022).
[39] J. Yang, S. Falletta, and A. Pasquarello, Range-separated hybrid functionals for accurate prediction of band gaps of extended systems, npj Comput. Mater. **9**, 108 (2023).
[40] A. Alkauskas, P. Broqvist, F. Devynck, and A. Pasquarello, Band offsets at semiconductor-oxide interfaces from hybrid density-functional calculations, Phys. Rev. Lett. **101**, 106802 (2008).
[41] W. Chen and A. Pasquarello, Band-edge positions in GW: Effects of starting point and self-consistency, Phys. Rev. B **90**, 165133 (2014).
[42] F. Ambrosio, Z. Guo, and A. Pasquarello, Absolute energy levels of liquid water, J. Phys. Chem. Lett. **9**, 3212 (2018).
[43] W. Chen and A. Pasquarello, Accuracy of GW for calculating defect energy levels in solids, Phys. Rev. B **96**, 020101(R) (2017).
[44] Z. Guo, F. Ambrosio, W. Chen, P. Gono, and A. Pasquarello, Alignment of redox levels at semiconductor–water interfaces, Chem. Mater. **30**, 94 (2018).
[45] G. Miceli, W. Chen, I. Reshetnyak, and A. Pasquarello, Nonempirical hybrid functionals for band gaps and polaronic distortions in solids, Phys. Rev. B **97**, 121112(R) (2018).
[46] J. F. Janak, Proof that $\frac{\partial E}{\partial n_i} = \epsilon$ in density-functional theory, Phys. Rev. B **18**, 7165 (1978).
[47] A. Miglio, V. Brousseau-Couture, E. Godbout, G. Antonius, Y.-H. Chan, S. G. Louie, M. Côté, M. Giantomassi, and X. Gonze, Predominance of non-adiabatic effects in zero-point renormalization of the electronic band gap, npj Comput. Mater. **6**, 167 (2020).
[48] M. Engel, H. Miranda, L. Chaput, A. Togo, C. Verdi, M. Marsman, and G. Kresse, Zero-point renormalization of the band gap of semiconductors and insulators using the projector augmented wave method, Phys. Rev. B **106**, 094316 (2022).

[49] M. Zacharias and F. Giustino, One-shot calculation of temperature-dependent optical spectra and phonon-induced band-gap renormalization, Phys. Rev. B **94**, 075125 (2016).
[50] H. Wang, A. Tal, T. Bischoff, P. Gono, and A. Pasquarello, Accurate and efficient band-gap predictions for metal halide perovskites at finite temperature, npj Comput. Mater. **8**, 237 (2022).
[51] J. R. Jasperse, A. Kahan, J. N. Plendl, and S. S. Mitra, Temperature dependence of infrared dispersion in ionic crystals LiF and MgO, Phys. Rev. **146**, 526 (1966).
[52] G. Peckham, The phonon dispersion relation for magnesium oxide, Proc. Phys. Soc. **90**, 657 (1967).
[53] M. J. L. Sangster, G. Peckham, and D. H. Saunderson, Lattice dynamics of magnesium oxide, J. Phys. C: Solid State Phys. **3**, 1026 (1970).
[54] C. W. M. Castleton and S. Mirbt, Finite-size scaling as a cure for supercell approximation errors in calculations of neutral native defects in InP, Phys. Rev. B **70**, 195202 (2004).
[55] C. W. M. Castleton, A. Höglund, and S. Mirbt, Managing the supercell approximation for charged defects in semiconductors: Finite-size scaling, charge correction factors, the band-gap problem, and the *ab initio* dielectric constant, Phys. Rev. B **73**, 035215 (2006).
[56] N. D. M. Hine, K. Frensch, W. M. C. Foulkes, and M. W. Finnis, Supercell size scaling of density functional theory formation energies of charged defects, Phys. Rev. B **79**, 024112 (2009).
[57] S. E. Taylor and F. Bruneval, Understanding and correcting the spurious interactions in charged supercells, Phys. Rev. B **84**, 075155 (2011).
[58] H.-P. Komsa, T. T. Rantala, and A. Pasquarello, Finite-size supercell correction schemes for charged defect calculations, Phys. Rev. B **86**, 045112 (2012).
[59] G. Onida, L. Reining, and A. Rubio, Electronic excitations: Density-functional versus many-body Green's-function approaches, Rev. Mod. Phys. **74**, 601 (2002).
[60] S. Albrecht, L. Reining, R. Del Sole, and G. Onida, *Ab initio* calculation of excitonic effects in the optical spectra of semiconductors, Phys. Rev. Lett. **80**, 4510 (1998).
[61] L. X. Benedict, E. L. Shirley, and R. B. Bohn, Optical absorption of insulators and the electron-hole interaction: An *ab initio* calculation, Phys. Rev. Lett. **80**, 4514 (1998).
[62] M. Rohlfing and S. G. Louie, Excitonic effects and the optical absorption spectrum of hydrogenated Si clusters, Phys. Rev. Lett. **80**, 3320 (1998).
[63] F. Fuchs, C. Rödl, A. Schleife, and F. Bechstedt, Efficient $\mathcal{O}(N^2)$ approach to solve the Bethe-Salpeter equation for excitonic bound states, Phys. Rev. B **78**, 085103 (2008).
[64] A. Tal, P. Liu, G. Kresse, and A. Pasquarello, Accurate optical spectra through time-dependent density functional theory based on screening-dependent hybrid functionals, Phys. Rev. Res. **2**, 032019 (2020).
[65] J. Sun and C. A. Ullrich, Optical properties of $CsCu_2X_3$(X = Cl, Br, and I): A comparative study between hybrid time-dependent density-functional theory and the Bethe-Salpeter equation, Phys. Rev. Mater. **4**, 095402 (2020).
[66] J. VandeVondele, M. Krack, F. Mohamed, M. Parrinello, T. Chassaing, and J. Hutter, QUICKSTEP: Fast and accurate density functional calculations using a mixed Gaussian and plane waves approach, Comput. Phys. Commun. **167**, 103 (2005).
[67] S. Goedecker, M. Teter, and J. Hutter, Separable dual-space Gaussian pseudopotentials, Phys. Rev. B **54**, 1703 (1996).
[68] J. VandeVondele and J. Hutter, Gaussian basis sets for accurate calculations on molecular systems in gas and condensed phases, J. Chem. Phys. **127**, 114105 (2007).
[69] P. Giannozzi, S. Baroni, N. Bonini, M. Calandra, R. Car, C. Cavazzoni, D. Ceresoli, G. L. Chiarotti, M. Cococcioni, I. Dabo, A. D. Corso, S. de Gironcoli, S. Fabris, G. Fratesi, R. Gebauer, U. Gerstmann, C. Gougoussis, A. Kokalj, M. Lazzeri, L. Martin-Samos *et al.*, QUANTUM ESPRESSO: A modular and open-source software project for quantum simulations of materials, J. Phys.: Condens. Matter **21**, 395502 (2009).
[70] D. R. Hamann, Optimized norm-conserving Vanderbilt pseudopotentials, Phys. Rev. B **88**, 085117 (2013).
[71] M. van Setten, M. Giantomassi, E. Bousquet, M. Verstraete, D. Hamann, X. Gonze, and G.-M. Rignanese, The PSEUDODOJO: Training and grading a 85 element optimized norm-conserving pseudopotential table, Comput. Phys. Commun. **226**, 39 (2018).
[72] A. A. Mostofi, J. R. Yates, G. Pizzi, Y.-S. Lee, I. Souza, D. Vanderbilt, and N. Marzari, An updated version of wannier90: A tool for obtaining maximally-localised Wannier functions, Comput. Phys. Commun. **185**, 2309 (2014).
[73] M. Iannuzzi, T. Chassaing, T. Wallman, and J. Hutter, Ground and excited state density functional calculations with the Gaussian and augmented-plane-wave method, Chimia **59**, 499 (2005).
[74] A. J. Read and R. J. Needs, Calculation of optical matrix elements with nonlocal pseudopotentials, Phys. Rev. B **44**, 13071 (1991).
[75] D. K. Smith and H. R. Leider, Low-temperature thermal expansion of LiH, MgO and CaO, J. Appl. Crystallogr. **1**, 246 (1968).
[76] W. Chen, G. Miceli, G.-M. Rignanese, and A. Pasquarello, Nonempirical dielectric-dependent hybrid functional with range separation for semiconductors and insulators, Phys. Rev. Mater. **2**, 073803 (2018).
[77] A. Tal, W. Chen, and A. Pasquarello, Vertex function compliant with the Ward identity for quasiparticle self-consistent calculations beyond *GW*, Phys. Rev. B **103**, L161104 (2021).
[78] S. Baba, I. Mori, and T. Nakano, Precise determination of the refractive index of sputtered MgO thin films in the visible light range, Vacuum **59**, 531 (2000).
[79] C. J. Liu and E. F. Sieckmann, Refractive index of calcium oxide, J. Appl. Phys. **37**, 2450 (1966).
[80] R. Whited, C. J. Flaten, and W. Walker, Exciton thermoreflectance of MgO and CaO, Solid State Commun. **13**, 1903 (1973).
[81] Y. Kaneko and T. Koda, New developments in IIa–VIb (alkaline-earth chalcogenide) binary semiconductors, J. Cryst. Growth **86**, 72 (1988).
[82] E. L. Albuquerque and M. S. Vasconcelos, Structural, electronics and optical properties of CaO, J. Phys.: Conf. Ser. **100**, 042006 (2008).
[83] S. Falletta, J. Wiktor, and A. Pasquarello, Finite-size corrections of defect energy levels involving ionic polarization, Phys. Rev. B **102**, 041115(R) (2020).

[84] T. Bischoff, I. Reshetnyak, and A. Pasquarello, Adjustable potential probes for band-gap predictions of extended systems through nonempirical hybrid functionals, Phys. Rev. B **99**, 201114(R) (2019).

[85] A. Alkauskas, P. Broqvist, and A. Pasquarello, Defect levels through hybrid density functionals: Insights and applications, Phys. Status Solidi (b) **248**, 775 (2011).

[86] M. A. L. Marques, J. Vidal, M. J. T. Oliveira, L. Reining, and S. Botti, Density-based mixing parameter for hybrid functionals, Phys. Rev. B **83**, 035119 (2011).

[87] L. Kronik and S. Kümmel, Piecewise linearity, freedom from self-interaction, and a Coulomb asymptotic potential: Three related yet inequivalent properties of the exact density functional, Phys. Chem. Chem. Phys. **22**, 16467 (2020).

[88] J. H. Skone, M. Govoni, and G. Galli, Self-consistent hybrid functional for condensed systems, Phys. Rev. B **89**, 195112 (2014).

[89] W. C. Ward and E. B. Hensley, Additive coloration of calcium oxide, Phys. Rev. **175**, 1230 (1968).

[90] L. Weston, H. Tailor, K. Krishnaswamy, L. Bjaalie, and C. G. Van de Walle, Accurate and efficient band-offset calculations from density functional theory, Comput. Mater. Sci. **151**, 174 (2018).

[91] J. L. Lyons and C. G. Van de Walle, Computationally predicted energies and properties of defects in GaN, npj Comput. Mater. **3**, 12 (2017).

[92] See Supplemental Material at http://link.aps.org/supplemental/10.1103/d78q-93fc for hybrid-functional atomic displacements at the O vacancy in MgO and the formation energies of the F centers in MgO and CaO, which also includes Refs. [96,97].

[93] M. Monge, R. González, J. Muñoz Santiuste, R. Pareja, Y. Chen, E. Kotomin, and A. Popov, Photoconversion of F^+ centers in neutron-irradiated MgO, Nucl. Instrum. Methods Phys. Res. Sec. B **166–167**, 220 (2000).

[94] A. Lushchik, A. Podelinska, V. Seeman, E. Shablonin, E. A. Kotomin, and V. N. Kuzovkov, Open questions on the thermal stability of primary electronic centers in irradiated MgO single crystals, J. Phys. Chem. C **129**, 2775 (2025).

[95] Materials Cloud platform, https://doi.org/1024435/materialscloudr6-np.

[96] C. G. Van de Walle and J. Neugebauer, First-principles calculations for defects and impurities: Applications to III-nitrides, J. Appl. Phys. **95**, 3851 (2004).

[97] C. Freysoldt, J. Neugebauer, and C. G. Van de Walle, Fully *ab initio* finite-size corrections for charged-defect supercell calculations, Phys. Rev. Lett. **102**, 016402 (2009).